

## Article

# Multi-Level Spectral Attention Network for Hyperspectral BRDF Reconstruction from Multi-Angle Multi-Spectral Images

Liyao Song<sup>1</sup> and Haiwei Li<sup>2,\*</sup> <sup>1</sup> Institute of Artificial Intelligence and Data Science, Xi'an Technological University, Xi'an 710021, China<sup>2</sup> Xi'an Institute of Optics and Precision Mechanics of Chinese Academy of Sciences, Xi'an 710119, China

\* Correspondence: lihaiwei@opt.ac.cn

**Abstract:** With the rapid development of hyperspectral applications using unmanned aerial vehicles (UAVs), the traditional assumption that ground objects exhibit Lambertian reflectance is no longer sufficient to meet the high-precision requirements for quantitative inversion and airborne hyperspectral data applications. Therefore, it is necessary to establish a hyperspectral bidirectional reflectance distribution function (BRDF) model suitable for the area of imaging. However, obtaining multi-angle information from UAV push-broom hyperspectral data is difficult. Achieving uniform push-broom imaging and flexibly acquiring multi-angle data is challenging due to spatial distortions, particularly under heightened roll or pitch angles, and the need for multiple flights; this extends acquisition time and exacerbates uneven illumination, introducing errors in BRDF model construction. To address these issues, we propose leveraging the advantages of multi-spectral cameras, such as their compact size, lightweight design, and high signal-to-noise ratio (SNR) to reconstruct hyperspectral multi-angle data. This approach enhances spectral resolution and the number of bands while mitigating spatial distortions and effectively captures the multi-angle characteristics of ground objects. In this study, we collected UAV hyperspectral multi-angle data, corresponding illumination information, and atmospheric parameter data, which can solve the problem of existing BRDF modeling not considering outdoor ambient illumination changes, as this limits modeling accuracy. Based on this dataset, we propose an improved Walthall model, considering illumination variation. Then, the radiance consistency of BRDF multi-angle data is effectively optimized, the error caused by illumination variation in BRDF modeling is reduced, and the accuracy of BRDF modeling is improved. In addition, we adopted Transformer for spectral reconstruction, increased the number of bands on the basis of spectral dimension enhancement, and conducted BRDF modeling based on the spectral reconstruction results. For the multi-level Transformer spectral dimension enhancement algorithm, we added spectral response loss constraints to improve BRDF accuracy. In order to evaluate BRDF modeling and quantitative application potential from the reconstruction results, we conducted comparison and ablation experiments. Finally, we solved the problem of difficulty in obtaining multi-angle information due to the limitation of hyperspectral imaging equipment, and we provide a new solution for obtaining multi-angle features of objects with higher spectral resolution using low-cost imaging equipment.



Academic Editor: Giancarlo Bellucci

Received: 27 December 2024

Revised: 25 February 2025

Accepted: 26 February 2025

Published: 28 February 2025

**Citation:** Song, L.; Li, H. Multi-Level Spectral Attention Network for Hyperspectral BRDF Reconstruction from Multi-Angle Multi-Spectral Images. *Remote Sens.* **2025**, *17*, 863. <https://doi.org/10.3390/rs17050863>

**Copyright:** © 2025 by the authors. Licensee MDPI, Basel, Switzerland. This article is an open access article distributed under the terms and conditions of the Creative Commons Attribution (CC BY) license (<https://creativecommons.org/licenses/by/4.0/>).

**Keywords:** UAV; BRDF; reconstruction; spectral attention network

## 1. Introduction

The BRDF is used to describe the reflectance characteristics of electromagnetic waves from natural surfaces [1,2]. The study of the BRDF typically relies on the acquisition of multi-angle data. This data collection can be categorized into three main platforms: satellite-borne [3], airborne, and ground-based remote sensing systems [4,5]. Ground-based multi-angle data acquisition equipment tends to be large, heavy, and complex to transport and assemble, and the measurement results are often susceptible to interference from self-shadowing effects. In contrast, UAVs have several advantages over satellite-borne and ground-based systems for multi-angle data acquisition. These advantages include greater operational flexibility, higher spatial resolution, lower operational costs, and the convenience of conducting ground-based synchronous auxiliary tests.

With the development of UAV-borne hyperspectral applications, the assumption that ground objects behave as Lambertian surfaces no longer satisfies the requirements for high-precision quantitative inversion and the application of airborne hyperspectral data [6]. Due to the low flying altitude and high spatial resolution of UAV-borne hyperspectral platforms, the effects of terrain undulations and the anisotropy of ground objects are more pronounced [7]. In the case of commonly used push-broom hyperspectral systems, images are typically acquired by maintaining a constant speed and straight flight path. However, platform instability, variations in flight attitude, imaging angle, and environmental changes lead to slight differences in the instantaneous field of view for each linear array, causing slight deviations in the observation direction. Then, each pixel within a single image is coupled with bidirectional reflectance from the ground surface, and the resulting effects are not uniform, which increases the complexity and uncertainty of BRDF modeling. Therefore, a more efficient method is required to establish the BRDF model.

High-quality input is fundamental for constructing a high-precision BRDF model. Traditional BRDF measurements are typically conducted under ideal conditions, such as clear, sunny days, and often require repeated measurements of fixed areas over extended periods. This approach is time-consuming and does not account for variations in illumination conditions during data acquisition. Errors caused by discrepancies in front-end radiance are carried through subsequent radiometric corrections in the BRDF model, becoming increasingly significant at lower solar altitude angles or over longer observation periods [8]. The definition of the BRDF does not impose specific environmental constraints, and as such, traditional BRDF measurements are generally based on the assumption that ambient illumination remains stable. However, in UAV imaging, environmental factors such as atmospheric conditions, cloud cover, and variation in water vapor content invariably affect the transmission of electromagnetic radiance. Consequently, the quantitative acquisition and modeling of the BRDF are influenced not only by the reflectance characteristics of ground objects but also by changes in the radiance characteristics of the imaging environment. This is further demonstrated by studies on multi-angle data collection and BRDF modeling conducted in both sunny and cloudy weather, which highlighted the need for greater radiance consistency in BRDF modeling data [9–15]. Multi-spectral cameras, characterized by their compactness, lightweight design, and high SNR, are particularly suitable for UAV-based BRDF research utilizing multi-angle multi-spectral imagery [16,17]. Reconstructing hyperspectral multi-angle data from multi-spectral multi-angle data enables the full utilization of multi-spectral imagery to capture the multi-angle features of objects, enhancing both spectral resolution and the number of spectral bands. This approach enables the acquisition of high-precision, high-quality multi-angle data at a lower cost [18]. The process of simulating high-dimensional data from low-dimensional inputs is inherently an underdetermined problem. In recent years, Transformer-based models have gained significant success in computer vision, particularly due to their multi-head

self-attention mechanism, which outperforms convolutional neural networks (CNNs) in capturing long-range dependencies and non-local self-similarity [19–22]. This ability helps address some of the limitations associated with CNN-based algorithms. Integrating BRDF reconstruction with deep learning techniques allows for leveraging the strengths of deep learning to address underdetermined problems while considering performance differences and spectral band variations across various remote sensing platforms. This approach facilitates data simulation from a data-driven perspective, thus meeting the BRDF modeling requirements for various imaging platforms, both ground-based and airborne.

The main contributions of this paper are summarized as follows.

(1) A hyperspectral dataset is collected using a UAV within the spectral range of 400–1000 nm. The dataset comprises 200 images along with corresponding illumination data, which are accurately linked to global positioning system (GPS) timestamps. Unlike existing datasets, our collection is specifically designed for UAV-based reconstruction that accounts for variations in outdoor solar illumination. This dataset offers valuable support for future research in outdoor spectral imaging, processing, and analysis.

(2) A method to enhance the accuracy of BRDF models is proposed by incorporating photometric correction to mitigate the radiance discrepancies in front-end data. The time-dependent photometric correction is incorporated into the BRDF modeling process, effectively eliminating the impact of radiometric variations in the front-end data during model construction. The BRDF model is developed using parameter values that accurately represent the bidirectional reflectance characteristics of ground objects. This approach effectively compensates for the impact of time-varying illumination on the multi-angle data acquisition process, ensuring the long-term accuracy of the BRDF model across extended time periods.

(3) Hyperspectral multi-angle data can be effectively reconstructed and generated by utilizing a multi-level Transformer-based spectral dimension enhancement algorithm combined with spectral response loss constraints. This approach expands the application potential of a multi-spectral BRDF and addresses the challenge of limited multi-angle information due to the constraints of hyperspectral imaging equipment. Consequently, it offers a novel solution for acquiring multi-angle features of ground objects with higher spectral resolution, utilizing low-cost imaging systems.

## 2. Methodology

### 2.1. Improvement of Walthall BRDF Model Based on Illumination Correction

The Walthall model is a typical BRDF statistical model that establishes a functional relationship between the bidirectional reflectance data and the observed zenith angle  $\theta_v$ , the observed azimuth angle  $\phi_v$ , and the solar azimuth angle  $\phi_i$ . The model often uses the difference between the latter two to represent the relative azimuth angle. The specific formula is as follows:

$$R(\theta_v, \phi_v, \phi_i) = a\theta_v^2 + b\theta_v \cos(\phi_v - \phi_i) + c \quad (1)$$

where  $a$ ,  $b$ , and  $c$  represent empirical coefficients.

However, Walthall ignored the effect of the solar zenith angle on the bidirectional reflectance of the ground objects. Based on this, Nilson and Kuusk [23] made improvements:

$$R(\theta_i, \theta_v, \phi_v, \phi_i) = a(\theta_i^2 + \theta_v^2) + b\theta_i^2\theta_v^2 + c\theta_i\theta_v \cos(\phi_v - \phi_i) + d \quad (2)$$

where  $d$  represent empirical coefficients.  $\theta_i$  is the solar zenith angle.

In order to enable the model to characterize the hotspot effect, Liang and Strahler [24] further added an exponential term that can characterize the hotspot effect:

$$R(\theta_i, \theta_v, \varphi_v, \varphi_i) = a(\theta_i^2 + \theta_v^2) + b\theta_i^2\theta_v^2 + c\theta_i\theta_v \cos(\varphi_v - \varphi_i) + d + c_1e^{-c_2 \tan(\pi-\xi)} \quad (3)$$

where  $c_1$ ,  $c_2$ , and  $\xi$  are undetermined coefficients.

The above model measures the entrance pupil radiance and uses the radiance of the whiteboard image as the reference to calculate the reflectance ratio:

$$\frac{L}{L_{\text{white}}} = R(\theta_i, \theta_v, \varphi_v, \varphi_i) \quad (4)$$

where  $L$  represents the entrance pupil radiance of each band observed by the sensor;  $L_{\text{white}}$  represents the radiance of the whiteboard.

Our research is based on the improved Walthall model, takes the radiance of the whiteboard at the time of imaging as the benchmark, introduces the illumination correction factor to correct the image, and, to some extent, compensates for the influence of Walthall's neglect of the solar zenith angle. The UAV remote sensing platform operated below the clouds, where solar illumination fluctuated rapidly due to cloud cover, affecting image brightness. To correct this, we use the atmospheric downwelling irradiance measuring device (DIMD) for continuous downward irradiance observation, with the cosine corrector positioned toward the zenith to minimize errors from varying observation angles. We interpolate DIMD data to match the push-broom line acquisition times of the UAV. The irradiance values are integrated into the hyperspectral imager's corresponding channels using a formula for radiance collection [25]. Illumination correction coefficients,  $k$ , for each band are derived by dividing the measured irradiance by the benchmark irradiance. The improved formula can be expressed as

$$\frac{L}{L_{\text{white}}} \cdot k = R'(\theta_i, \theta_v, \varphi_v, \varphi_i) \quad (5)$$

$$R'(\theta_i, \theta_v, \varphi_v, \varphi_i) = k \left( a(\theta_i^2 + \theta_v^2) + b\theta_i^2\theta_v^2 + c\theta_i\theta_v \cos(\varphi_v - \varphi_i) + d + c_1e^{-c_2 \tan(\pi-\xi)} \right) \quad (6)$$

where  $R'$  represents the reflectance with illumination correction.

## 2.2. BRDF Reconstruction Model Based on Multi-Level Spectral Attention Mechanism

Based on the improved Walthall model, when acquiring multi-angle data, we employed a multi-level spectral reconstruction model to enhance the spectral resolution of BRDF data during multi-angle data acquisition. This network was proposed by Cai et al. [26] and performs well in the task of hyperspectral reconstruction. The overall structure of the network is shown in Figure 1.

Figure 1a shows a single-level spectral-wise transformer (SST) network. The embedding layer in SST is a  $3 \times 3$  convolution, the downsampling operation adopts a  $4 \times 4$  convolution, and the upsampling operation employs a  $2 \times 2$  transposed convolution. Figure 1b shows a multi-level spectral reconstruction network. The entire network uses three SST modules. In order to avoid information loss during downsampling operation, the entire module uses skip-layer connections. The upsampling and downsampling processes involve transferring feature combination information through feature permutation.

Traditional visual Transformers divide images evenly into multiple sub-blocks along the spatial dimension to form tokens. However, hyperspectral data exhibit high spatial similarity across sparse channels, making it more computationally efficient to calculate self-attention along the spectral channel dimension rather than the spatial dimension. Based

on this insight, Spectral-wise Multi-head Self-Attention (S-MSA) treats the feature map of each spectral channel as a token and calculates its self-attention features. This approach significantly enhances the focus on spectral features during spectral reconstruction. In this module, each spectral channel’s feature is used as a token to facilitate spectral dimension reconstruction. The structure of this module is illustrated in Figure 2a.

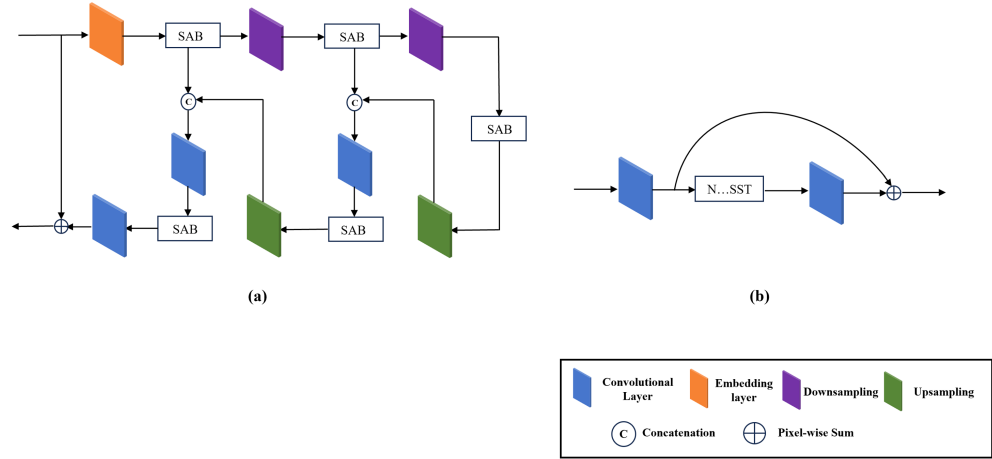


**Figure 1.** Multi-level BRDF spectral reconstruction network. (a) Single-level spectral transformer module SST; (b) Multi-level spectral reconstruction network.

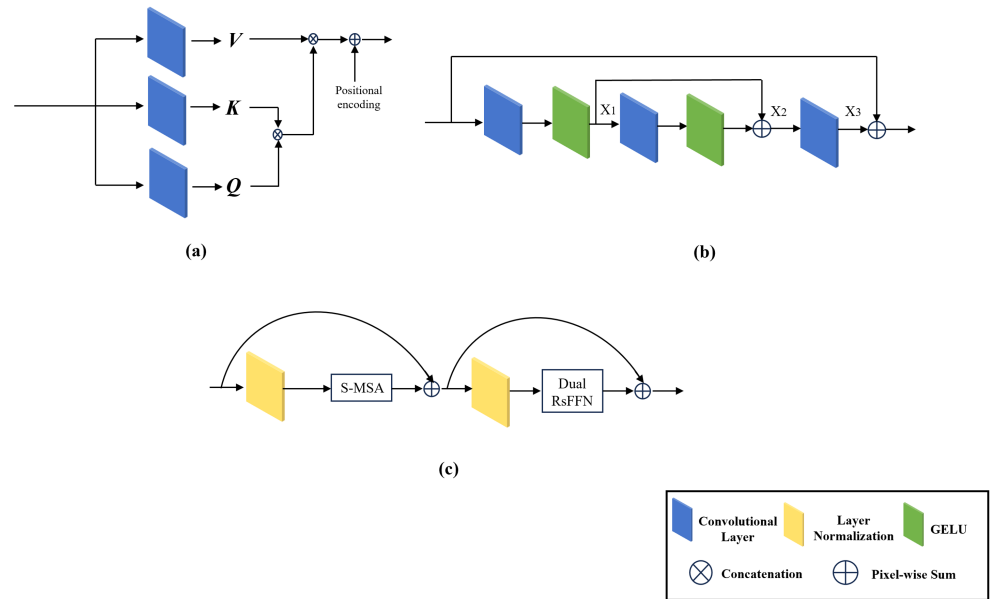


**Figure 2.** The structure of each component in the SST module. (a) Spectral Multi-Head Attention Module S-MSA; (b) Dual RsFFN; (c) Spectral Attention Module SAB.

Assume  $X_{in} \in \mathbb{R}^{H \times W \times C}$  is the input. First,  $X_{in}$  is transformed along the spectral dimension and shaped into  $C$  tokens to obtain  $X_{cube} \in \mathbb{R}^{HW \times C}$ . Then,  $X_{cube}$  enters three branches and uses  $C$  channels convolution to obtain  $Q$  branch  $X_Q \in \mathbb{R}^{HW \times C}$ ,  $K$  branch  $X_K \in \mathbb{R}^{HW \times C}$ , and  $V$  branch  $X_V \in \mathbb{R}^{HW \times C}$ .

Since the input multi-spectral information and each spectral dimension of the hyper-spectral have different degrees of correlation, directly employing the multi-head attention method cannot learn the input spectral features well. The formula of the single-head self-attention model is as follows:

$$SA = X_V \left( \text{soft max} \left( \sigma X_K^T X_Q \right) \right) \tag{7}$$

where  $\mathbf{X}_K^T$  represents the transposed matrix of  $\mathbf{X}_K$ .

The entire  $S - \text{MSA}$  can be expressed as follows:

$$S - \text{MSA}(\mathbf{X}_{\text{in}}) = (\text{concat}_{\text{head}=1}^N(SA)\mathbf{w} + \text{GELU}(\mathbf{X}_V)) \quad (8)$$

where  $\mathbf{w}$  is an external spectral parameter with a learnable dimension of  $1 \times C$  that is initialized to 0. Finally, the output of  $S - \text{MSA}$  is reshaped to obtain the output feature map  $\mathbf{X}_{\text{out}} \in \mathbb{R}^{H \times W \times C}$  of the  $N$  heads.

The traditional Transformer is followed by a feed-forward network (FFN). Considering that the convolutional layer has good local context perception, we designed a dual residual feed-forward neural network called Dual RsFFN, as shown in Figure 2b. Given a module input,  $X' \in \mathbb{R}^{C \times H \times W}$ , in RsFFN, a convolution of  $1 \times 1$  is first used to expand  $X'$  to a higher dimension,  $X_1 \in \mathbb{R}^{rC \times H \times W}$ , where  $r$  is the ratio of the number of expansion channels, which is set to 4 in this study. Then, a convolution of  $3 \times 3$  is used to encode the information of the adjacent pixel positions of  $X_1$ , and it is summed with  $X_1$  to obtain  $X_2 \in \mathbb{R}^{rC \times H \times W}$ . Finally,  $X_2$  is remapped to the initial input dimension of  $X_3 \in \mathbb{R}^{C \times H \times W}$  through the  $1 \times 1$  convolution layer, and the final output is summed with the input. The whole process increases the permutation and combination of features by expanding the channel ratio, and it then removes redundant features by using a convolution of  $1 \times 1$  to reduce the dimension. GELU is used as the activation function after each convolution layer. The above process can be expressed as

$$X_1 = \text{GELU}(\text{Conv}_1(X')) \quad (9)$$

$$X_2 = X_1 + \text{GELU}(\text{Conv}_2(X_1)) \quad (10)$$

$$X_3 = X' + \text{GELU}(\text{Conv}_3(X_2)) \quad (11)$$

where  $\text{Conv}_1$  and  $\text{Conv}_3$  denote  $1 \times 1$  convolution, and  $\text{Conv}_2$  represents  $3 \times 3$  convolution. Finally,  $S - \text{MSA}$  and Dual RsFFN form the spectral attention module SAB, as shown in Figure 2c.

### 2.3. Loss Function of the Reconstruction Model

The entire model BRDF reconstruction network can be optimized by minimizing the MRAE between the reconstructed BRDF data  $\mathbf{I}_{REC}$  and the corresponding ground truth (GT) data  $\mathbf{I}_{HSI}$ .

Previous CNN-based spectral reconstruction models fit RGB to hyperspectral image (HSI) mapping and rarely consider integrating camera spectral sensitivity into spectral reconstruction to achieve more accurate reconstruction. Li et al. [27] proposed the camera spectral response (CSR) function based on the fact that a given CSR function can be applied to the reconstructed HSI as a more refined constraint. Therefore, the loss function is a linear combination of two terms that can more finely represent the difference between the resampled RGB of the GT image and the reconstructed HSI. The CSR function is as follows:

$$\mathcal{L}_{\text{CSR}} = \frac{1}{WHN} \sum_{n=1}^N \sum_{i=1}^W \sum_{j=1}^H \left| \left( \mu(\mathbf{I}_{\text{HSI}}^{ijn}) - \mu(\mathbf{I}_{\text{REC}}^{ijn}) \right) \right| \quad (12)$$

$$\mathcal{L}_{\text{Total}} = \mathcal{L}_{\text{MRAE}} + \eta \mathcal{L}_{\text{CSR}} \quad (13)$$

where  $\mu$  represents the spectral response function of CIE-1964;  $\eta$  is a hyperparameter, which is empirically set to 10.

### 3. Experimental Results and Analysis

#### 3.1. Experimental Data and Settings

The push-broom hyperspectral imaging system and the illumination measurement system are used for multi-angle hyperspectral data collection in this experiment. The imaging system used in this study comprised a lightweight UAV, a MicroHSI™410SHARK hyperspectral imager, a RedEdge multi-spectral imager, and a DJI Ronin MX stabilization platform. The UAV platform employed is a M600pro DJI, known for its cost-effectiveness and user-friendly operation. It has a maximum payload capacity of 6.0 kg and a total weight of 10 kg, including the battery. The UAV can withstand wind speeds up to 8 m/s and achieve a maximum horizontal flight speed of 18 m/s. Its hover time without a payload is 38 min, and it operates within an environmental temperature range of  $-10$  to  $40$  °C. Considering the endurance of the UAV and the time limitations for BRDF observation, the azimuth angle range covered in this study spans from  $0^\circ$  to  $360^\circ$ , with a step size of  $30^\circ$ . The zenith angle observation range is from  $0^\circ$  to  $20^\circ$ , with a step size of  $5^\circ$ . Automatic observations at specified positions, angles, and altitudes are achieved through the design of the flight route.

During the collection of multi-angle data, the experiment utilizes a multi-rectangular overlapping flight path (Figure 3). This flight route addresses the limitations of traditional circular flight paths, which are not suitable for push-broom hyperspectral imaging, while also enhancing data collection efficiency. To maintain a stable imaging distance of 50 m, flights with a  $0^\circ$  zenith angle and the multi-rectangular overlapping flight path were conducted separately. By stabilizing the gimbal's side swing, observations of different zenith angles are achieved for each rectangular route. An atmospheric downlink irradiance measurement device is positioned in a flat, open area within the experimental zone. This device, consisting of a spectrometer, a cosine corrector, and a storage unit, collects time-varying illumination data simultaneously with the multi-angle data. Different grayscale targets (reflectance values of 70%, 50%, 40%, 20%, 10%, and 5%) and standard whiteboards are sequentially placed in the target area for subsequent reflectance conversion and BRDF model validation. The test duration, number of flights, and atmospheric conditions are summarized in Table 1 and Figure 4.

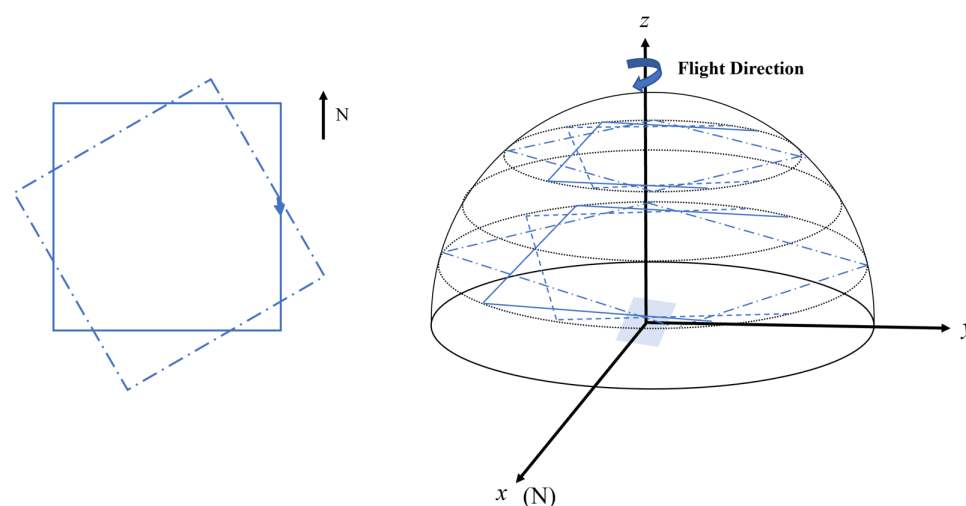


**Figure 3.** UAV nested multi-rectangular flight routes.

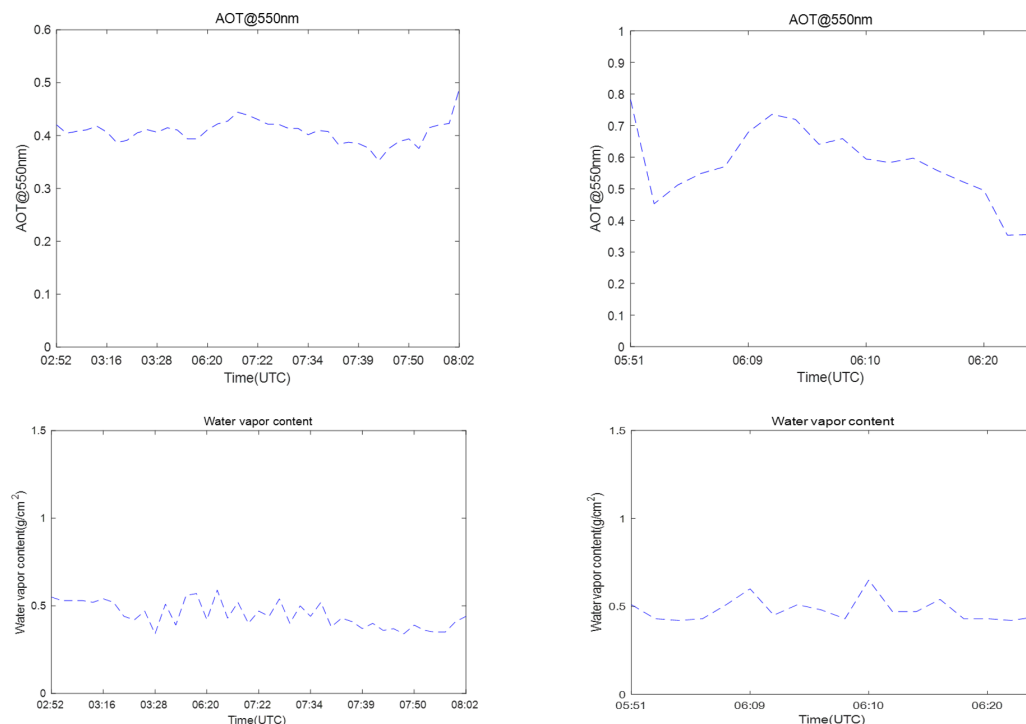


**Figure 4.** Changes in aerosol and water vapor content on the day of the experiment (left column: the first day; right column: the second day).

**Table 1.** Basic statistics of UAV tests.

Time	Flights	Solar Zenith Angle (°)	Solar Azimuth (°)
20230303	7	0–56	103–235
20230304	3	32–60	124–271

The process of multi-angle data collection is outlined as follows (taking a flight altitude of 50 m as an example):

- (1) The UAV flies at an altitude of 50 m and collects data at a 0° observation zenith angle. At this time, the flight direction is from south to north, and the stable gimbal moves vertically downward to complete the push-scan of the space dimension;
- (2) Lower the altitude of the UAV and collect observations at a 5° zenith angle. At this time, the flight route follows the planned rectangular route: adjust the stabilization gimbal’s side swing angle to 5° and fly each rectangle in a clockwise direction to complete the collection of all observation azimuth angles at the zenith angle;
- (3) Decrease the flight altitude, adjust the lateral movement distance, stabilize the gimbal side swing angle to 10°, and continue to complete the acquisition of all observation azimuth angles under the zenith angle in a clockwise direction;
- (4) Continue to adjust the flight altitude, lateral displacement, and lateral swing angle, and repeat the above steps to complete the collection of the remaining observation zenith angle information;
- (5) Observations are conducted over multiple days at different times to collect data corresponding to varying solar zenith and azimuth angles. Finally, the data are reviewed, and additional flights are conducted if necessary to ensure comprehensive coverage.

When observing at different zenith angles, it is necessary to program and preset the flight route and adjust the flight altitude and lateral movement distance of the UAV; the observation angle of the UAV at the moment of imaging is shown in Figure 5, where the

UAV can descend to the next fixed altitude and automatically adjust the lateral displacement distance according to the latitude and longitude coordinates.

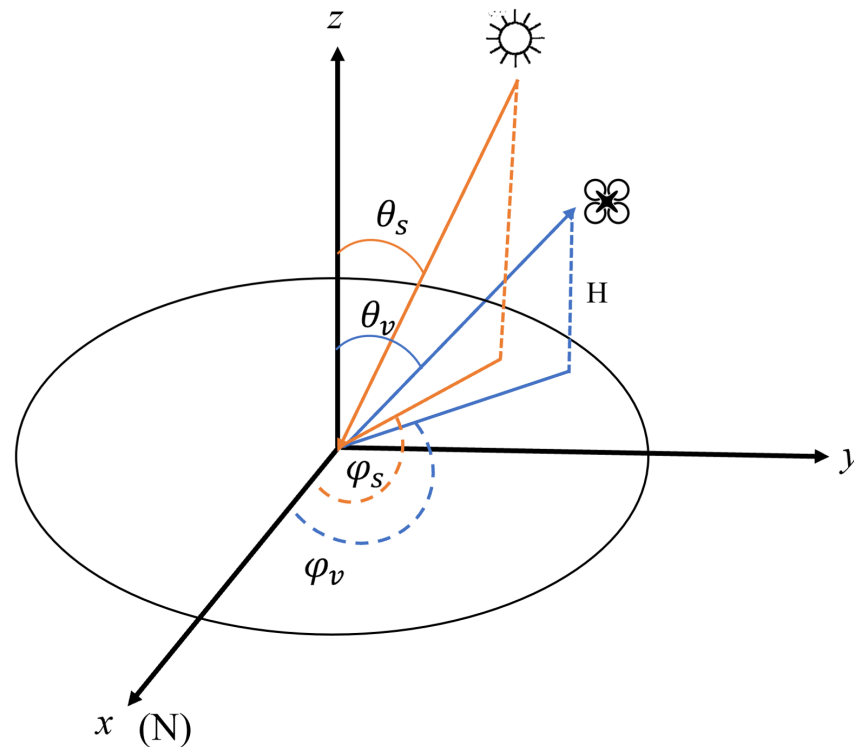


**Figure 5.** Schematic diagram of observation angles at the moment of UAV imaging.

The calculation formulas for the flight altitude and lateral distance of the UAV in the test are as follows:

$$h = H * \cos \theta_v \quad (14)$$

$$h = H * \sin \theta_v \quad (15)$$

where  $H$  is the initial altitude,  $\theta_v$  is the zenith angle of the UAV,  $h$  is the altitude corresponding to different zenith angles, and  $s$  is the lateral displacement distance corresponding to different zenith angles. The corresponding relationship between the lateral displacement distance, altitude, and side swing angle in the experiment is shown in Table 2.

**Table 2.** Flight parameter correspondence table.

Zenith Angle (°)	Flight Altitude (m)	Distance of Lateral Displacement (m)
0	50	0
5	49.8	4.35
10	49.2	8.68
15	48.2	12.94
20	46.9	17.10
25	45.3	21.13

On the basis of sufficient data collection, BRDF modeling and evaluation work are carried out. The data processing workflow is illustrated in Figure 6. Due to the influence of UAV take-off and landing times, as well as turning and attitude changes during flight, invalid data may be generated. Therefore, the first step is to eliminate redundant data. Next, the illumination correction coefficients are calculated and applied using the time when each flight strip passes over the standard whiteboard. Finally, atmospheric corrections are

applied individually to each edge of the overlapping rectangles in each flight strip, ensuring that the edges of the rectangles are minimally affected by variations in illumination and observation geometry.

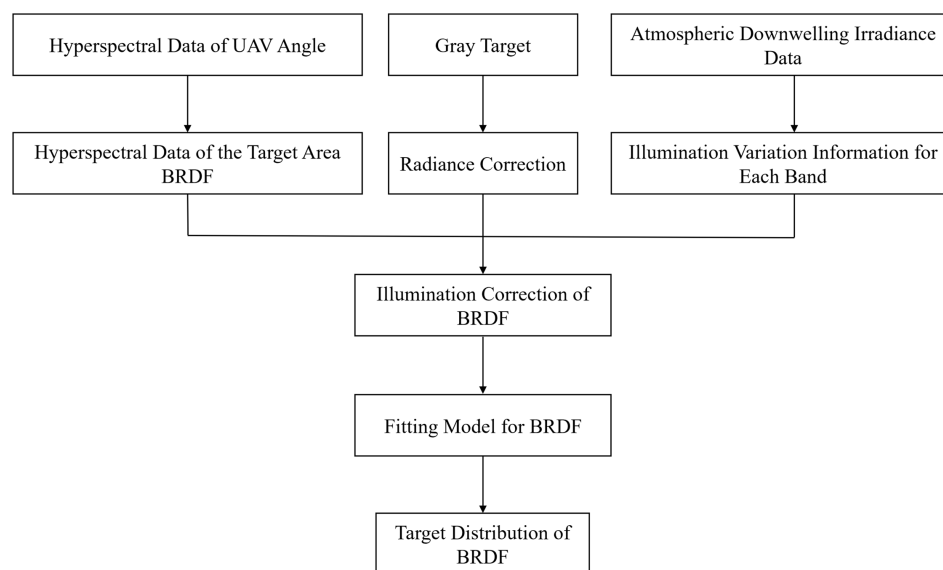


**Figure 6.** Processing flow of multi-angle data.

Our experiment employs deep learning for the spectral reconstruction of the BRDF. The UAV hyperspectral training set uniformly crops  $64 \times 64$  pixel, three-band multi-spectral, and 31-band hyperspectral samples from the original dataset. The batch size of the model is 20, and the parameters of the Adam optimization algorithm are  $a$  and  $b$ . The initial learning rate is 0.0004, and the cosine annealing scheme is used for 20 cycles of learning. Finally, the test dataset is input into the trained network to obtain the reconstructed hyperspectral image. The GPU is NVIDIA RTX 3090, and the development environment is Pytorch.

### 3.2. Comparative Experiment and Analysis

In order to analyze the reconstruction effect of the hyperspectral reconstruction model, this section compares it with advanced reconstruction algorithms such as HSCNN+ [28], HRNet [29], EDSR [30], HDNet [31], MIRnet [32], MPRNet [33], and MST++ [26]. The results are shown in Figure 7.

We mainly list the reconstruction results under the same observation azimuth angle when the observation zenith angle,  $\theta_v$ , is  $5^\circ$ ,  $10^\circ$ , and  $15^\circ$ , respectively. The main ground objects are targets with different gray levels. A comparison of the image reconstruction results from different methods reveals that all approaches have yielded favorable outcomes. In terms of texture details, the spatial relative positioning of each image pixel is well preserved, indicating that the BRDF acquisition angle characteristics have been effectively maintained without introducing errors in angle information during subsequent BRDF modeling. From a color perspective, some algorithms exhibit slight color discrepancies in the reconstruction. This is primarily due to deviations in one of the three bands of the true-color composite image. These deviations tend to increase as the observation zenith angle increases, suggesting that the spectral curve reconstruction accuracy of these algorithms needs further improvement. In addition, the color information of algorithms such as MST++, MPRNet, and MIRnet has little variation, and these can be used as the preferred algorithms for BRDF reconstruction. From the perspective of feature information, such as targets and shadows in the image, some algorithms, such as HDNet and HRNet, have shadows of varying degrees, and the reconstruction results of EDSR, MIRNet, HDNet,

HRNet, etc., have grayscale anomalies in the high reflectance target area, indicating that these algorithms need to optimize the local attention module when reconstructing the BRDF image in order to further improve the accuracy of local reconstruction.

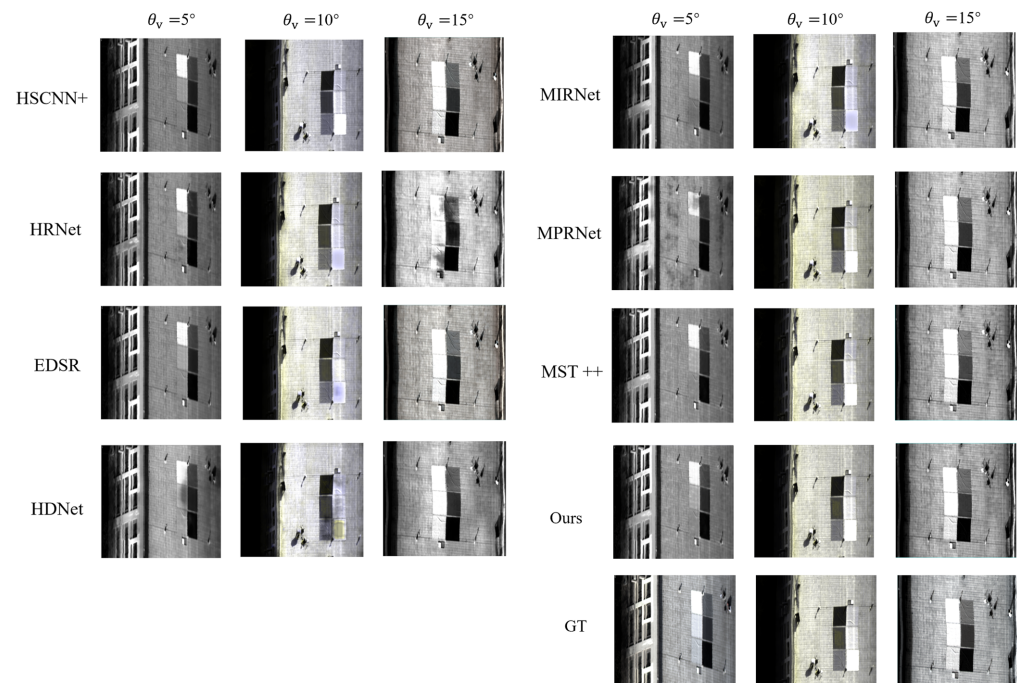


**Figure 7.** Comparison of true color results of BRDF data reconstructed using different methods at different observation zenith angles.

Figure 8 presents a comparison of the mean spectral curves obtained from the spectral reconstruction of BRDF test data under different illumination conditions. The first row displays the reconstructed hyperspectral curves, with the spectral reconstruction results for  $5^\circ$ ,  $10^\circ$ , and  $15^\circ$  zenith angles shown from left to right. The spectral curve reconstructed for the target area was selected for analysis. The spectral curve reconstructed at a  $10^\circ$  zenith angle closely matches the real data. The second row illustrates the hyperspectral error curves. In the error analysis, the algorithm presented in this study exhibits relatively low errors for the first 22 bands, demonstrating a closer alignment with the GT spectral curve.

Figure 9 shows the heat map visualization results of the BRDF test data in the 5-*th* and 15-*th* bands of the HSCNN+, HRNet, EDSR, HDNet, MIRnet, MPRNet, and MST++ algorithms and the proposed algorithm, with observation zenith angles of  $5^\circ$ ,  $10^\circ$ , and  $15^\circ$ .

From top to bottom, the heat maps show the spectral reconstruction results for input multi-spectral data for HSCNN+, HRNet, MST++, and the algorithm proposed in this study. The results demonstrate that the proposed algorithm consistently delivers satisfactory reconstruction outcomes, regardless of the observation zenith angles ( $5^\circ$ ,  $10^\circ$ , or  $15^\circ$ ). Notably, at a  $5^\circ$  observation zenith angle, the reconstruction closely approximates the GT, with the entire heat map appearing predominantly dark blue. For an observation zenith angle of  $10^\circ$ , the heat map reveals relatively larger reconstruction errors in the darker areas of the original image. For instance, a small portion of the heat map for the HDNet algorithm approaches red, indicating that the comparison algorithm fails to accurately capture the hyperspectral attributes corresponding to the input sample area, resulting in substantial deviations between the reconstructed and actual results. Although the BRDF spectral reconstruction algorithm proposed in this study exhibits varying degrees of error at different locations, the heat map shows significant improvement compared to the other algorithms.

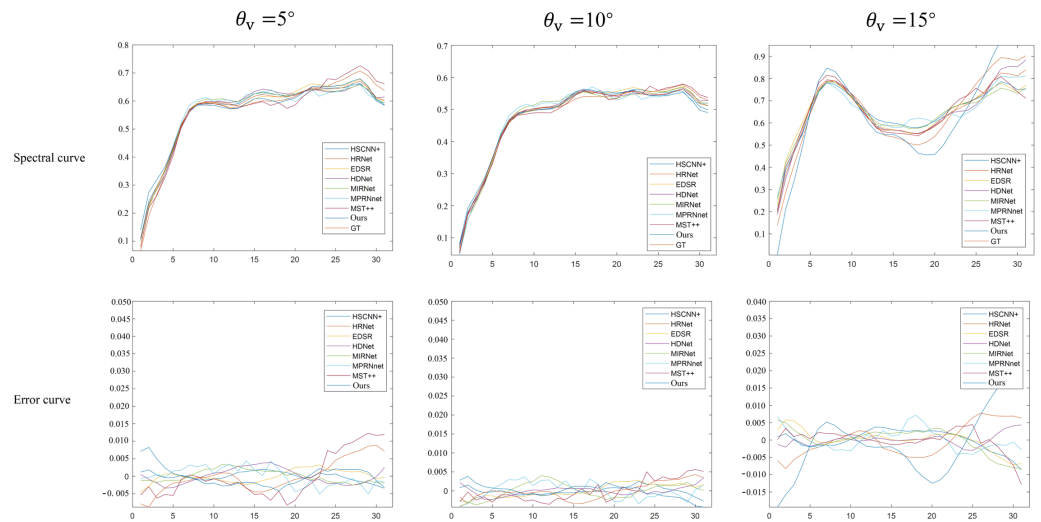


**Figure 8.** Comparison of mean spectral curves and error curves reconstructed by different BRDF methods at different angles.

The experimental results indicate that the error value for the 15-*th* band is higher than that for the 5-*th* band. This discrepancy is primarily due to the lower SNR of the bands closer to the beginning of the hyperspectral data, which introduces interference during the reconstruction process and leads to larger errors in the reconstructed data. In contrast, starting from the 15-*th* band, the higher SNR of the subsequent bands improves reconstruction quality. By analyzing the error heat maps, it is evident that the hyperspectral BRDF data reconstructed using the proposed algorithm exhibit the lowest error values compared to the other algorithms, both for the 5-*th* and 15-*th* bands. The results demonstrate that the proposed algorithm achieves excellent performance regardless of whether the SNR is low or high, indicating its robustness across different conditions.

Additionally, Table 3 presents the experimental results of the BRDF test set, evaluated using two performance metrics: RMSE and MRAE. The results demonstrate that the proposed algorithm outperforms the comparison algorithms in both metrics, achieving the lowest MRAE of 0.3377. This indicates that incorporating spectral response loss as a constraint in the reconstruction network enhances the accuracy of spectral dimension reconstruction for BRDF data. To provide a more intuitive comparison, this paper also includes a comparison of the parameter counts for different algorithms; the parameter counts are in millions (M). Notably, since the spectral response loss is integrated into the network of the proposed method based on MST++, the parameter count remains consistent with that of MST++. This highlights the efficiency advantage of MST++, which is the main factor regarding selection in the spectral reconstruction of multi-angle data.

**Table 3.** Quantitative comparison of different reconstruction methods on the test set.

Method	RMSE	MRAE	Parameter Calculation Amount (M/Millions)
HSCNN+	0.0866	0.5472	4.65
HRNet	0.0815	0.4997	31.70
EDSR	0.0621	0.4804	2.42
HDNet	0.0530	0.3751	2.66
MIRNet	0.0488	0.3539	3.75
MPRNet	0.0488	0.3469	3.62
MST++	0.0469	0.3385	1.62
Ours	0.0461	0.3377	1.62

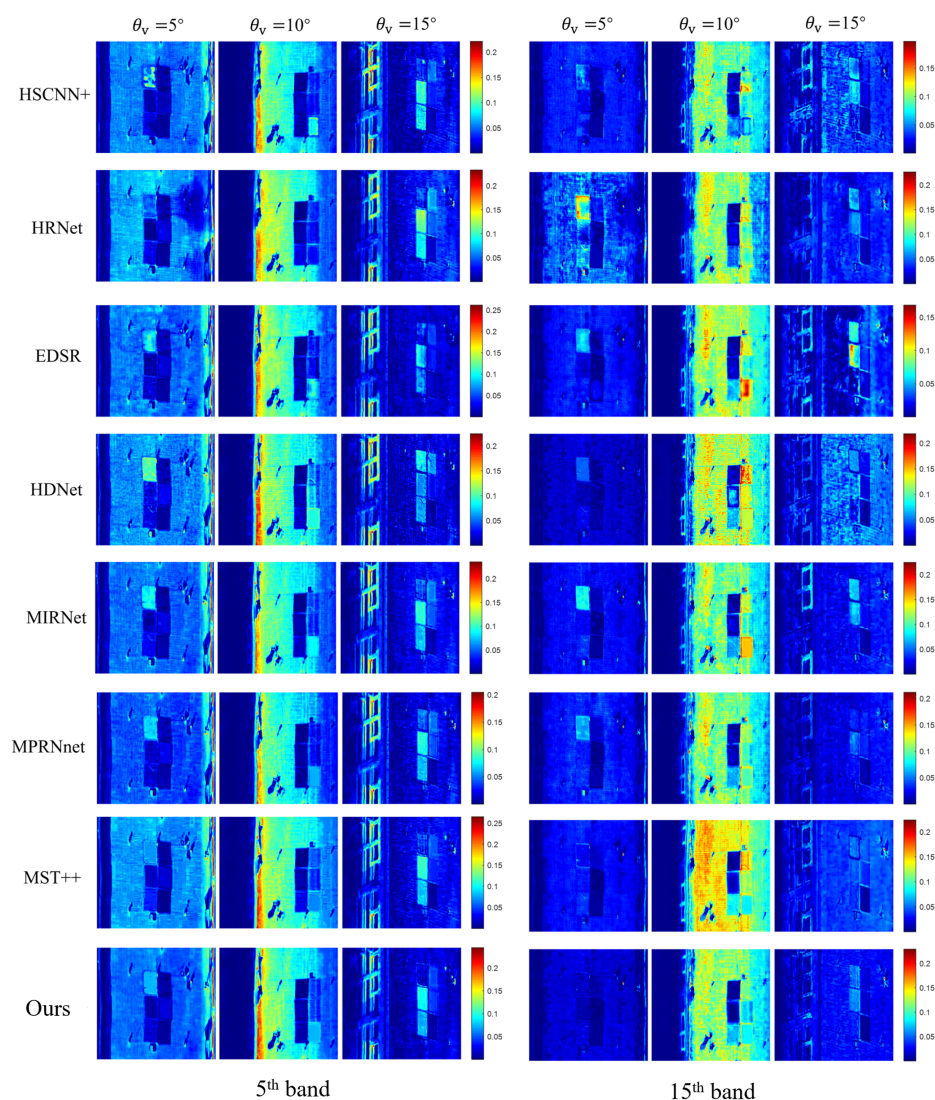


**Figure 9.** Error heat map comparison of the reconstruction results of different reconstruction methods in the 5-th and 15-th bands.

### 3.3. Ablation Experiment and Analysis

For the SST module, we set the number of stackings to 2, 3, 4, and 5 to explore the effect of model depth on reconstruction. We can see that as  $N$  increases, MRAE and RMSE will decrease to varying degrees, but the corresponding network parameters will also increase. After increasing to 4, the accuracy will no longer improve. It is demonstrated that when stacking three modules, high-precision reconstruction can be maintained. As can be seen from Table 4, as the number of stacked modules increases, the number of parameters also increases.

**Table 4.** Quantitative comparison of different numbers of SST on the test set.

Number of SST	RMSE	MRAE	Parameter Calculation Amount (M)
$N = 2$	0.0465	0.3402	1.08
$N = 3$	0.0461	0.3377	1.62
$N = 4$	0.0489	0.3685	2.16
$N = 5$	0.0493	0.3798	2.70

### 3.4. Quantitative Application

After analyzing and comparing the multi-angle spectral reconstruction experiment, we verified the reconstruction results via quantitative application. Our method was primarily used to model the BRDF of the reconstructed multi-angle data and to compare it with the results of the multi-angle BRDF model. In the experiment, five different kinds of target reflectance in five bands are selected for illustration.

When modeling the BRDF, we utilized the Walthall model based on illumination improvement to model the BRDF and reduce the impact of illumination on the BRDF. To more intuitively illustrate the effect of illumination correction on the Walthall model, we present polar coordinate diagrams for different grayscale targets across various bands.

To minimize the introduction of additional sources of error, we selected the hyperspectral data for analysis. After converting the radiance to reflectance, the data were input into the Walthall model, both with and without illumination correction, to generate multi-angle enhanced data. By examining the distribution of these data, we can intuitively assess the improvement in the Walthall model with illumination correction, thereby highlighting the critical importance of accurate BRDF modeling. The distribution results of the BRDF model data with/without illumination are shown in Figure 10.

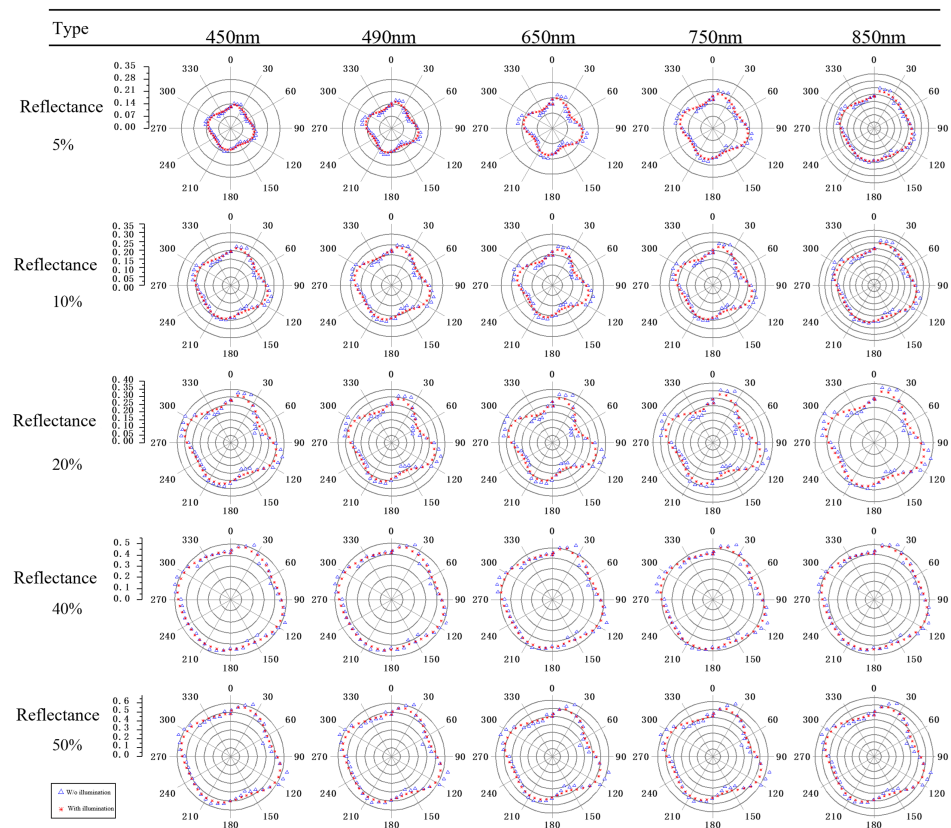


**Figure 10.** Comparison of Walthall model data distribution with/without considering the illumination variation.

The outer perimeter of the polar coordinates represents different observation azimuths ranging from  $0^\circ$  to  $360^\circ$ , and the radial axis corresponds to the reflectance values of the data. The blue triangles indicate the multi-angle data distribution without considering illumination, whereas the red stars represent the multi-angle distribution after illumination correction. As observed from Figure 10, the data dispersion is significantly reduced when illumination is considered, with the values predominantly distributed along the circumference. The transitions and changes are much smoother. In contrast, when illumination is

not considered, the data transitions at the inflection points appear less smooth and natural, with some values exhibiting substantial fluctuations. After the illumination correction, the range of these fluctuations is notably reduced.

To more intuitively demonstrate the impact of illumination correction, Table 5 presents a comparison of the standard deviation and mean of the BRDF data across five selected bands, both with and without illumination correction. After applying the illumination correction, the standard deviation and mean for each band were significantly reduced. This indicates that environmental factors such as weather changes (including illumination, cloud cover, and atmospheric conditions) can influence the accuracy of the collected BRDF data and the resulting model. Given the relatively low flight altitude of the UAV, the radiance transmitted through the atmosphere encompasses nearly the entire atmospheric column. Although this study employed drone-based hyperspectral data collection as an alternative to ground-based platforms, the process remains susceptible to a range of factors. These influences are highly variable and random, underscoring the necessity of synchronized measurements from either ground or drone platforms to mitigate such error sources during both data acquisition and modeling.

**Table 5.** Standard deviation with/without considering illumination.

Reflectance	Without Considering Illumination						With Considering Illumination					
	450 nm	490 nm	650 nm	750 nm	850 nm	Avg.	450 nm	490 nm	650 nm	750 nm	850 nm	Avg.
5%	0.02	0.02	0.02	0.02	0.03	0.02	0.01	0.01	0.01	0.01	0.02	0.01
10%	0.03	0.03	0.03	0.03	0.04	0.03	0.01	0.01	0.02	0.02	0.02	0.02
20%	0.05	0.05	0.06	0.06	0.07	0.06	0.03	0.03	0.03	0.04	0.04	0.03
40%	0.03	0.04	0.05	0.05	0.05	0.04	0.02	0.02	0.03	0.03	0.03	0.03
50%	0.06	0.06	0.08	0.09	0.08	0.07	0.03	0.04	0.05	0.05	0.05	0.04

When collecting BRDF multi-angle data, we selected targets with favorable isotropic characteristics. By comparing the data distribution of the targets in different bands and different gray levels, it can be seen that illumination is an important source of error in BRDF modeling. Adding illumination correction will reduce the error of BRDF data, thereby improving the accuracy of the BRDF model's description of the multi-angle features of ground objects.

After studying the influence of illumination on the distribution of BRDF data and improving it, we reveal the BRDF modeling results of each grayscale target based on the improved Walthall model, as shown in Figure 11. In the polar coordinate diagram, the outer circle of  $0^\circ$ – $360^\circ$  represents different observation azimuths, the radial axis represents different observation zenith angles, and the color represents the reflectance value of each grayscale target at different angles. We randomly selected five evenly distributed bands of 450 nm, 490 nm, 650 nm, 750 nm, and 850 nm to show the results.

Figure 11 presents the BRDF modeling results of hyperspectral data after incorporating illumination correction, using polar coordinates to provide a more intuitive representation of the data distribution and underlying patterns. By comparing the grayscale reflectance at different levels, it is evident that with increasing reflectance, the reflectance of each band at an observation azimuth of  $90^\circ$  tends to rise, exhibiting a pronounced hotspot effect. When comparing different spectral bands, it is observed that as the wavelength increases, the multi-angle distribution of reflectance for low-reflectance targets shows minimal change, and the reflectance distribution for high-reflectance targets exhibits more pronounced variations. These findings indicate that for uniform and flat objects under clear weather conditions, higher reflectance leads to a more pronounced bidirectional reflectance effect, which becomes more evident at longer wavelengths.

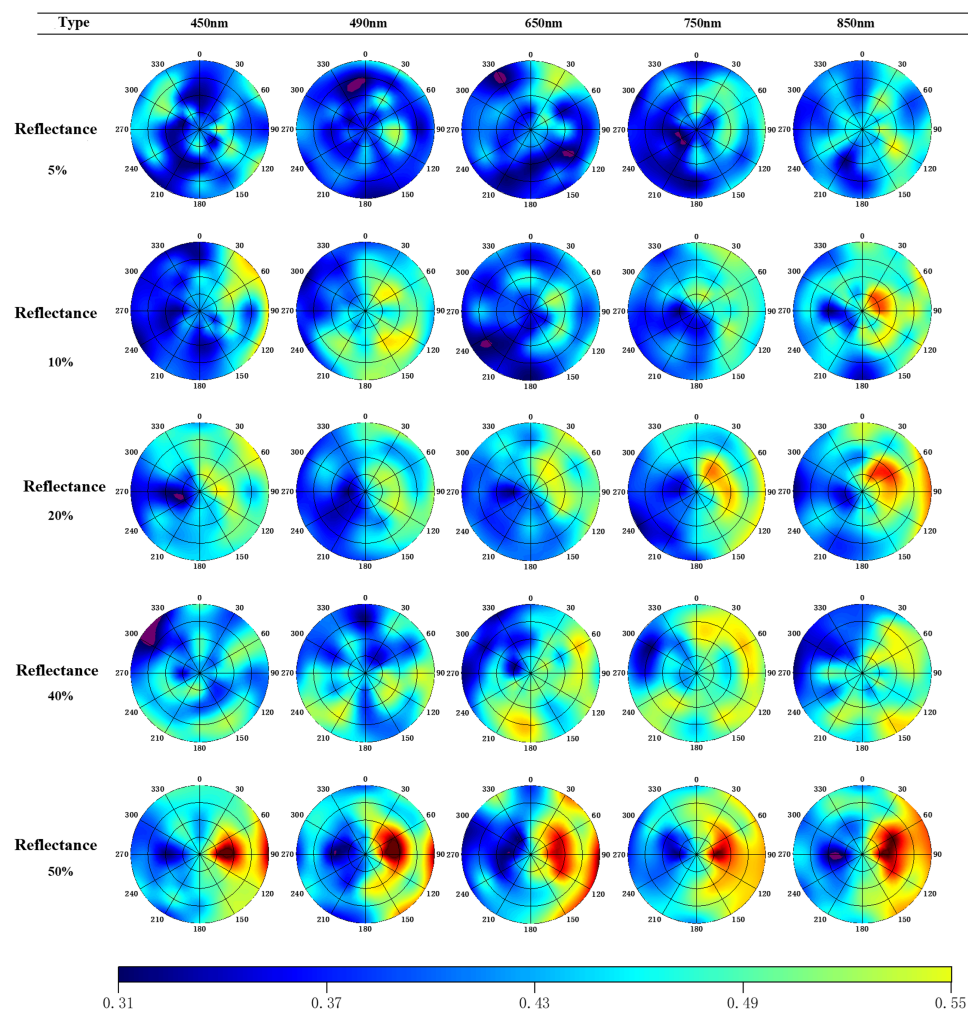


**Figure 11.** Hyperspectral BRDF modeling with illumination correction Walthall model.

We utilized the spectral reconstruction results along with the Walthall model, incorporating illumination correction, to model the BRDF, and the results are presented in Figure 12. The BRDF results derived from the spectral reconstruction data more effectively capture the multi-angle characteristics across various grayscale levels and wavelengths. The direction of the hotspot effect is clearly visible in the overall polar coordinate diagram. A comparison of different bands reveals that, with increasing wavelength, the multi-angle distribution of low-reflectance targets changes slowly, while the distribution for high-reflectance targets exhibits more significant variations. When the spectral device has a limited number of bands, spectral reconstruction can enhance the spectral dimension, increasing the number of bands and thereby providing a more comprehensive representation of the multi-angle reflectance characteristics of ground objects across a broader spectral range.

Figure 13 illustrates the absolute difference between the spectral reconstruction BRDF model and the hyperspectral BRDF model. The color scale represents the magnitude of the error, with brighter colors indicating larger errors. In the brightest regions of the image, the error value is predominantly controlled within 0.09, and most of the errors are below 0.07. The reflectance errors for different targets show an increasing trend with the rise in observation zenith angle, as indicated by the radial axis of the polar coordinates. This pattern suggests that the primary source of error in BRDF reconstruction is spectral variability during multi-angle observation. As the observation angle changes, the hyperspectral camera captures corresponding variations in the data, which reflect the combined

effects of observation angle, environmental factors, and the multi-angle characteristics of ground objects.

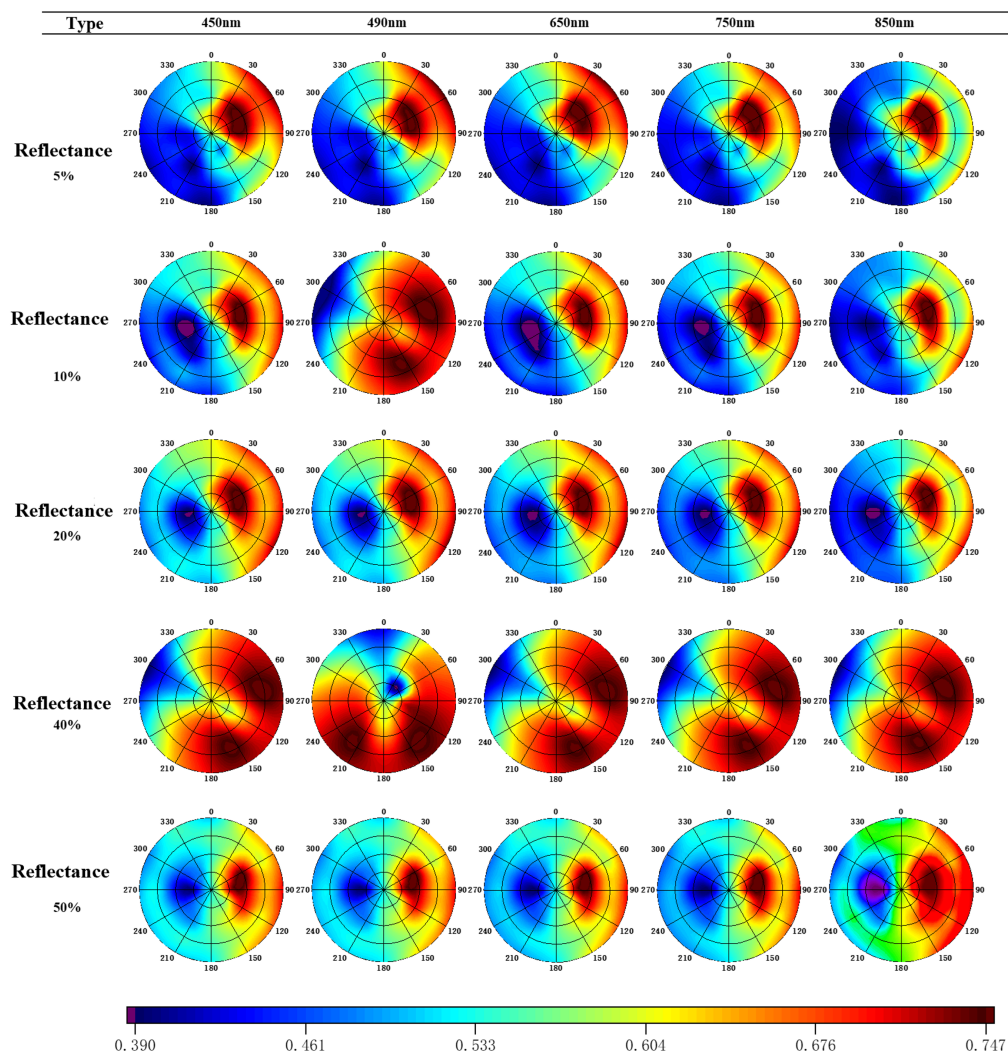


**Figure 12.** Multi-angle spectral reconstruction BRDF modeling considering the illumination-corrected Walthall model.

The process of generating high-dimensional spectral data from low-dimensional inputs via spectral reconstruction involves deep learning to model how spectral data change with angle and the corresponding increase in spectral band data. In addition to expanding the number of spectral bands per pixel, spectral reconstruction also incorporates the learning of spatial structures and texture information. Throughout this process, factors such as radiance transmission, angular characteristics, proximity effects, temperature variations, and environmental changes are inter-related, collectively influencing and constraining the accuracy of BRDF reconstruction.

To facilitate a more intuitive comparison of the error changes, we further statistically analyzed the errors, as shown in Table 6. The statistical analysis of the mean errors for different reflectance values across each band reveals that, as reflectance increases, the error mean generally follows a trend of gradual increase. This trend is particularly pronounced at 450 nm and 850 nm, which are located at the spectral extremes of the detector’s response range. Based on the detector’s response characteristics, it can be observed that the SNR at the ends of the spectral range is slightly lower compared to the central bands.

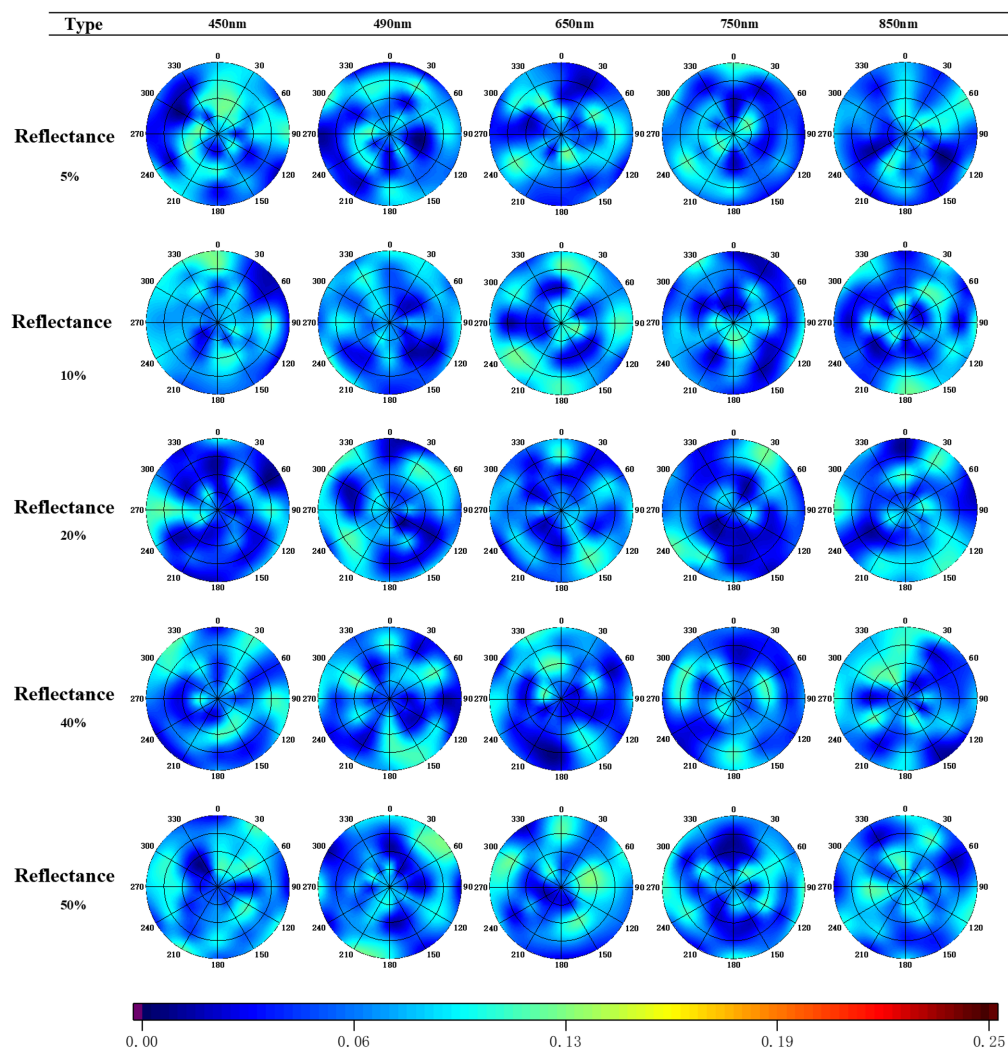


Figure 13. Error analysis comparison between spectral reconstruction BRDF model and hyperspectral BRDF model.

Table 6. Statistics of mean error between spectral reconstruction BRDF model and hyperspectral BRDF.

Reflectance	450 nm	490 nm	650 nm	750 nm	850 nm	Avg.
5%	0.05	0.06	0.06	0.05	0.05	0.05
10%	0.06	0.06	0.07	0.05	0.07	0.06
20%	0.07	0.06	0.07	0.06	0.07	0.07
40%	0.06	0.07	0.06	0.06	0.08	0.07
50%	0.09	0.06	0.07	0.08	0.09	0.08

We considered the error source of illumination during our research, mainly reducing the impact of downlink illumination (direct + diffuse) on BRDF spectral reconstruction. This reduces the spectral variation caused by the mismatch of the spatiotemporal dimensions during the measurement, BRDF modeling, and reconstruction processes, improving the robustness of the algorithm.

According to the above analysis, the accuracy of obtaining the BRDF of ground objects using the spectral reconstruction method for spectral dimension enhancement still needs to be improved. Future research can consider the influence of the atmosphere on the radiance transmission of different bands, combine deep learning algorithms to reconstruct the spectral dimension more accurately, and improve the modeling accuracy of the BRDF.

## 4. Conclusions

This paper presents a comprehensive collection of UAV hyperspectral multi-angle data, along with corresponding illumination and atmospheric parameters. These data address the issue that existing BRDF models often neglect variations in outdoor solar illumination, which can adversely affect the accuracy of modeling. By building upon this dataset, we propose an improved Walthall model that incorporates illumination factors. This enhancement effectively optimizes radiance consistency across multi-angle BRDF data, mitigating errors introduced by illumination changes and ultimately improving BRDF modeling accuracy.

Furthermore, we employed Transformer-based methods for spectral reconstruction. By increasing the number of spectral bands through spectral dimension enhancement, we modeled the BRDF based on the reconstructed spectral data. The multi-level Transformer spectral dimension enhancement algorithm was augmented with a spectral response loss constraint to further refine BRDF accuracy. To evaluate the effectiveness and quantitative potential of the reconstructed images, we conducted ablation experiments, analyzing various reflectance levels and spectral bands. In the future, we will fully exploit the multi-angle observation potential of the existing instruments.

**Author Contributions:** Conceptualization, H.L. and L.S.; methodology, L.S. and H.L.; supervision, H.L.; formal analysis, L.S. and H.L.; writing—original draft preparation, L.S.; writing—review and editing, H.L. All authors have read and agreed to the published version of the manuscript.

**Funding:** National Key Research and Development Program of China (No. 2022YFF1300201); General Special Scientific Research Program Project of the Shaanxi Provincial Department of Education (No. 24JK0481); National Natural Science Foundation of China (No. 42101380).

**Data Availability Statement:** The original contributions presented in the study are included in the article, further inquiries can be directed to the corresponding author.

**Conflicts of Interest:** The authors declare no conflict of interest. The funders had no role in the design of the study; in the collection, analyses, or interpretation of data; in the writing of the manuscript, or in the decision to publish the results.

## References

1. Zhang, H.; Jiao, Z.T.; Dong, Y.D.; Li, J.Y.; Li, X.W. Albedo Retrieved from BRDF Archetype and Surface Directional Reflectance. *Remote Sens.* **2015**, *19*, 355–367. [[CrossRef](#)]
2. Zhu, W.; You, D.; Wen, J.; Tang, Y.; Gong, B.; Han, Y. Evaluation of Linear Kernel-Driven BRDF Models over Snow-Free Rugged Terrain. *Remote Sens.* **2023**, *15*, 786. [[CrossRef](#)]
3. Han, Y.; Wen, J.; Xiao, Q.; Bao, Y.; Chen, X.; Liu, Q.; He, M. Review of the Land Surface BRDF Inversion Methods based on Remotely Sensed Satellite Data. *Natl. Remote Sens. Bull.* **2023**, *27*, 2024–2040. [[CrossRef](#)]
4. Li, H.; Zhang, H.; Zhang, B.; Chen, Z.; Yang, M.; Zhang, Y. A Method Suitable for Vicarious Calibration of a UAV Hyperspectral Remote Sensor. *IEEE J. Sel. Top. Appl. Earth Obs. Remote Sens.* **2015**, *8*, 3209–3223. [[CrossRef](#)]
5. Tao, B.C.; Hu, X.Q.; Yang, L.K.; Zhang, L.; Chen, L.; Xu, N.; Wang, L.; Wu, R.Q.; Zhang, D.F.; Zhang, P. BRDF Feature Observation Method and Modeling of Desert Site based on UAV Platform. *Natl. Remote Sens. Bull.* **2021**, *25*, 1964–1977. [[CrossRef](#)]
6. Jiao, Z.; Zhang, H.; Dong, Y.; Liu, Q.; Xiao, Q.; Li, X. An Algorithm for Retrieval of Surface Albedo From Small View-Angle Airborne Observations Through the Use of BRDF Archetypes as Prior Knowledge. *IEEE J. Sel. Top. Appl. Earth Obs. Remote Sens.* **2015**, *8*, 3279–3293. [[CrossRef](#)]
7. Wu, S.; Wen, J.; Liu, Q.; You, D.; Yin, G.; Lin, X. Improving Kernel-Driven BRDF Model for Capturing Vegetation Canopy Reflectance with Large Leaf Inclinations. *IEEE J. Sel. Top. Appl. Earth Obs. Remote Sens.* **2020**, *13*, 2639–2655. [[CrossRef](#)]
8. Song, F.; Fan, W.; Liu, Q.; Xu, X. A Method of Acquiring BRDF of Objects in the Field. *J. Remote Sens. Beijing* **2020**, *13*, 239–255.

9. Zhang, C.B.; Yang, S.T.; Zhao, C.S.; Lou, H.Z.; Zhang, Y.C.; Bai, J.; Wang, Z.W.; Guan, Y.B.; Zhang, Y. Topographic Data Accuracy Verification of Small Consumer UAV. *J. Remote Sens.* **2018**, *22*, 185–195. [[CrossRef](#)]
10. Chang, Y.X.; Jiao, Z.T.; Dong, Y.D.; Zhang, X.N.; He, D.D.; Yin, S.Y.; Cui, L.; Ding, A.X. Parameterization and Correction of Hotspot Parameters of Ross-Li Kernel Driven Models on POLDER Dataset. *J. Remote Sens.* **2019**, *23*, 661–672. [[CrossRef](#)]
11. Dong, Y.D.; Jiao, Z.T.; Zhang, H.; Li, J.Y.; Jiao, G.P.; Shi, H.Y. Efficient Algorithm for Improving the Hotspot Effect of the Operational MODIS BRDF Product. *J. Remote Sens.* **2014**, *18*, 804–825.
12. Guo, J.; Jiao, Z.T.; Ding, A.X.; Dong, Y.D.; Zhang, X.N.; Cui, L.; Yin, S.Y.; Chang, Y.X.; Xie, R. Evaluation of Three BRDF Models' Performance Using Spaceborne POLDER Snow Data. *Natl. Remote Sens. Bull.* **2020**, *26*, 2060–2072. [[CrossRef](#)]
13. Li, J.; Jiao, Z.; Zhang, H.; Dong, Y. Variance of Bidirectional Reflectance and Its Application Using Operational MODIS BRDF Model. *J. Remote Sens.* **2020**, *13*, 2639–2655.
14. Qiu, F.; Huo, J.W.; Zhang, Q.; Chen, X.H.; Zhang, Y.G. Observation and Analysis of Bidirectional and Hotspot Reflectance of Conifer Forest Canopies with a Multiangle Hyperspectral UAV Imaging Platform. *Natl. Remote Sens. Bull.* **2021**, *25*, 1013–1024. [[CrossRef](#)]
15. Wang, L.; Hu, X.Q.; Xu, N.; Chen, L.; Zhang, P.; Xu, H.L. Research on Construction of Directional Reflectance Reference Model for Desert Stable Earth Targets. *Natl. Remote Sens. Bull.* **2023**, *27*, 2270–2282. [[CrossRef](#)]
16. Crucil, G.; Zhang, H.; Pauly, K.; Van Oost, K. A Semi-Empirical Anisotropy Correction Model for UAS-based Multispectral Images of Bare Soil. *Remote Sens.* **2022**, *14*, 537. [[CrossRef](#)]
17. Wang, Z.; Li, H.; Wang, S.; Song, L.; Chen, J. Methodology and Modeling of UAV Push-Broom Hyperspectral BRDF Observation Considering Illumination Correction. *Remote Sens.* **2024**, *16*, 543. [[CrossRef](#)]
18. Fu, L.; Gao, F.; Wu, J.; Li, R.; Karkee, M.; Zhang, Q. Application of Consumer RGB-D Cameras for Fruit Detection and Localization in Field: A Critical Review. *Comput. Electron. Agric.* **2020**, *177*, 105687. [[CrossRef](#)]
19. Ma, Q.; Jiang, J.; Liu, X.; Ma, J. Reciprocal Transformer for Hyperspectral and Multispectral Image Fusion. *Inf. Fusion* **2024**, *104*, 102148. [[CrossRef](#)]
20. Han, K.; Wang, Y.; Chen, H.; Chen, X.; Guo, J.; Liu, Z.; Tao, D. A Survey on Vision Transformer. *IEEE Trans. Pattern Anal. Mach. Intell.* **2022**, *45*, 87–110. [[CrossRef](#)] [[PubMed](#)]
21. Benzenati, T.; Kallel, A.; Kessentini, Y. STF-Trans: A Two-Stream Spatiotemporal Fusion Transformer for Very High Resolution Satellites Images. *Neurocomputing* **2024**, *563*, 126868. [[CrossRef](#)]
22. Vaswani, A. Attention is All You Need. *Adv. Neural Inf. Process. Syst.* **2017**, *30*, 105687.
23. Nilson, T.; Kuusk, A. A Reflectance Model for the Homogeneous Plant Canopy and Its Inversion. *Remote Sens. Environ.* **1989**, *27*, 157–167. [[CrossRef](#)]
24. Liang, S.; Strahler, A.H. Retrieval of Surface BRDF from Multiangle Remotely Sensed Data. *Remote Sens. Environ.* **1994**, *50*, 18–30. [[CrossRef](#)]
25. Song, L.; Li, H.; Chen, T.; Chen, J.; Liu, S.; Fan, J.; Wang, Q. An integrated solution of UAV push-broom hyperspectral system based on geometric correction with MSI and radiation correction considering outdoor illumination variation. *Remote Sens.* **2022**, *14*, 6267. [[CrossRef](#)]
26. Cai, Y.; Lin, J.; Lin, Z.; Wang, H.; Zhang, Y.; Pfister, H.; Van Gool, L. MST++: Multi-Stage Spectral-Wise Transformer for Efficient Spectral Reconstruction. In Proceedings of the IEEE/CVF Conference on Computer Vision and Pattern Recognition Workshops, New Orleans, LA, USA, 19–23 June 2022.
27. Li, J.; Wu, C.; Song, R.; Li, Y.; Liu, F. Adaptive weighted attention network with camera spectral sensitivity prior for spectral reconstruction from RGB images. In Proceedings of the IEEE/CVF Conference on Computer Vision and Pattern Recognition Workshops, Seattle, WA, USA, 14–19 June 2020.
28. Shi, Z.; Chen, C.; Xiong, Z.; Liu, D.; Wu, F. HSCNN+: Advanced CNN-Based Hyperspectral Recovery from RGB Images. In Proceedings of the IEEE/CVF Conference on Computer Vision and Pattern Recognition Workshops, Salt Lake City, UT, USA, 18–22 June 2018; pp. 939–947.
29. Zhao, Y.; Po, L.M.; Yan, Q.; Liu, W.; Lin, T. Hierarchical Regression Network for Spectral Reconstruction from RGB Images. In Proceedings of the IEEE/CVF Conference on Computer Vision and Pattern Recognition Workshops, Seattle, WA, USA, 14–19 June 2020; pp. 422–423.
30. Lim, B.; Son, S.; Kim, H.; Nah, S.; Mu Lee, K. Enhanced Deep Residual Networks for Single Image Super-Resolution. In Proceedings of the IEEE/CVF Conference on Computer Vision and Pattern Recognition Workshops, Honolulu, HI, USA, 21–26 July 2017; pp. 136–144.
31. Hu, X.; Cai, Y.; Lin, J.; Wang, H.; Yuan, X.; Zhang, Y.; Van Gool, L. HDNet: High-Resolution Dual-Domain Learning for Spectral Compressive Imaging. In Proceedings of the IEEE/CVF Conference on Computer Vision and Pattern Recognition, New Orleans, LA, USA, 19–24 June 2022; pp. 17542–17551.

32. Zamir, S.W.; Arora, A.; Khan, S.; Hayat, M.; Khan, F.S.; Yang, M.H.; Shao, L. Learning Enriched Features for Real Image Restoration and Enhancement. In Proceedings of the 16th European Conference on Computer Vision, Glasgow, UK, 23–28 August 2020; pp. 492–511.
33. Zamir, S.W.; Arora, A.; Khan, S.; Hayat, M.; Khan, F.S.; Yang, M.H.; Shao, L. Multi-Stage Progressive Image Restoration. In Proceedings of the IEEE/CVF Conference on Computer Vision and Pattern Recognition, Nashville, TN, USA, 20–25 June 2021; pp. 14821–14831.

**Disclaimer/Publisher’s Note:** The statements, opinions and data contained in all publications are solely those of the individual author(s) and contributor(s) and not of MDPI and/or the editor(s). MDPI and/or the editor(s) disclaim responsibility for any injury to people or property resulting from any ideas, methods, instructions or products referred to in the content.